

# Graphene supported plasmonic photocatalyst for hydrogen evolution in photocatalytic water splitting

G P Singh<sup>1,2</sup>, K M Shrestha<sup>3</sup>, A Nepal<sup>2</sup>, K J Klabunde<sup>3</sup> and C M Sorensen<sup>2</sup>

<sup>1</sup> Centre for Nanotechnology, Central University of Jharkhand, Ranchi-835205, Jharkhand, India

<sup>2</sup> Department of Physics, Kansas State University, Manhattan, KS 66506, USA

<sup>3</sup> Department of Chemistry, Kansas State University, Manhattan, KS 66506, USA

E-mail: [gpsinghcuj@gmail.com](mailto:gpsinghcuj@gmail.com) and [gajendra.singh@cuj.ac.in](mailto:gajendra.singh@cuj.ac.in)


Received 13 February 2014, revised 27 April 2014

Accepted for publication 30 April 2014

Published 11 June 2014

## Abstract

It is well known that the noble metal nanoparticles show active absorption in the visible region because of the existence of the unique feature known as surface plasmon resonance (SPR). Here we report the effect of plasmonic Au nanoparticles on the enhancement of the renewable hydrogen (H<sub>2</sub>) evolution through photocatalytic water splitting. The plasmonic Au/graphene/TiO<sub>2</sub> photocatalyst was synthesized in two steps: first the graphene/TiO<sub>2</sub> nanocomposites were developed by the hydrothermal decomposition process; then the Au was loaded by photodeposition. The plasmonic Au and the graphene as co-catalyst effectively prolong the recombination of the photogenerated charges. This plasmonic photocatalyst displayed enhanced photocatalytic H<sub>2</sub> evolution for water splitting in the presence of methanol as a sacrificial reagent. The H<sub>2</sub> evolution rate from the Au/graphene co-catalyst was about 9 times higher than that of a pure graphene catalyst. The optimal graphene content was found to be 1.0 wt %, giving a H<sub>2</sub> evolution of 1.34 mmol (i.e., 26  $\mu\text{molh}^{-1}$ ), which exceeded the value of 0.56 mmol (i.e., 112  $\mu\text{molh}^{-1}$ ) observed in pure TiO<sub>2</sub>. This high photocatalytic H<sub>2</sub> evolution activity results from the deposition of TiO<sub>2</sub> on graphene sheets, which act as an electron acceptors to efficiently separate the photogenerated charge carriers. However, the Au loading enhanced the H<sub>2</sub> evolution dramatically and achieved a maximum value of 12 mmol (i.e., 2.4  $\text{mmolh}^{-1}$ ) with optimal loading of 2.0 wt% Au on graphene/TiO<sub>2</sub> composites. The enhancement of H<sub>2</sub> evolution in the presence of Au results from the SPR effect induced by visible light irradiation, which boosts the energy intensity of the trapped electron as well as active sites for photocatalytic activity.

 Online supplementary data available from [stacks.iop.org/NANO/25/265701/mmedia](http://stacks.iop.org/NANO/25/265701/mmedia)

Keywords: graphene, TiO<sub>2</sub>, hydrogen, gold, water splitting

(Some figures may appear in colour only in the online journal)

## 1. Introduction

Improvement in hydrogen (H<sub>2</sub>) evolution through photo-induced water splitting is emerging as a viable choice to meet the need for clean, sustainable energy for various practical applications and to resolve environmental problems [1–5]. The sustainable and efficient evolution of H<sub>2</sub> requires a stable and efficient catalytic system for water oxidation (to form molecular oxygen), and this is the more

challenging half-reaction in the overall water splitting [6, 7]. After intensive study, the semiconductors having a conduction band (CB) edge sufficiently more negative than the reduction potential of water (or protons) and that remain stable when in contact with water have been considered as appropriate catalyst materials. The interfacial area between the catalyst and liquid water should also be large enough to allow water dissociation to take place at a high specific rate [7, 8].

Titanium dioxide ( $\text{TiO}_2$ ) has been found to be a good photocatalyst among semiconductors for  $\text{H}_2$  evolution because of its wide band gap (3.2 eV), appreciable photoactivity under UV light irradiation, stability, nontoxicity, inexpensiveness, and availability [9, 10]. However,  $\text{TiO}_2$  is poorly active for  $\text{H}_2$  production as a result of fast electron-hole recombination and large over-potential characteristics. The most promising and viable ways to overcome these drawbacks are the deposition of metal nanoparticles on bare  $\text{TiO}_2$  or the self-doping of  $\text{TiO}_2$  with compatible materials [11–14].

Recently, graphene, a two-dimensional  $\text{sp}^2$  network of carbon, has been shown to possess outstanding mechanical strength and thermal conductivity ( $5000 \text{ W m}^{-1} \text{ K}^{-1}$ ) and exhibits an exceptionally high theoretical specific surface area ( $2600 \text{ m}^2 \text{ g}^{-1}$ ), high transparency, structural flexibility, chemical stability, and superior mobility of charge carriers ( $200\,000 \text{ cm}^2 \text{ V}^{-1} \text{ s}^{-1}$ ), [10, 15–17]. On the basis of these extraordinary properties, graphene has been considered another useful material for  $\text{H}_2$  production because it (i) provides a support for anchoring well-dispersed metallic or oxide nanoparticles; (ii) works as a highly conductive matrix for enabling good contact throughout the matrix; (iii) induces an easy electron transfer from the CB of semiconductors to graphene because of the large energy level offset formed at the interface, leading to an efficient charge separation; and (iv) acts as an efficient co-catalyst for  $\text{H}_2$  evolution because of its large specific surface area and superior electron mobility [18–22]. However, the  $\text{H}_2$  evolution activity of graphene as co-catalyst is still limited and needs to be further enhanced from the viewpoint of practical applications and commercial benefits.

In this context, a few bimetallic systems, namely Au/Pd core-shell nanoparticles, polymer protected Pt/Ru bimetallic clusters, bimetallic Au/Pt systems, and nonmetal elements such as S, N, and C immobilized on  $\text{TiO}_2$ , have been investigated for  $\text{H}_2$  production through photo-induced water splitting [10, 13, 23–26]. It is observed that the heterogeneous catalysts deliver good performances in hydrogenation reactions as a result of longer electron mobility as well as surface ensemble effects. In addition, the versatile properties of Au nanoparticles, such as the capacity to alter the physicochemical properties, surface plasmon resonance (SPR), conductivity, and redox behavior, have proved Au to be a useful material for the range of applications leading to improvement in catalytic properties [27].

In this paper we report the properties of visible-region, SPR-responsive, Au-nanoparticle-loaded, graphene-supported  $\text{TiO}_2$  nanocomposite photocatalysts for enhanced  $\text{H}_2$  evolution through water splitting in the presence of methanol as a scavenger. The loading of Au on the graphene and  $\text{TiO}_2$  surface is done as a means of using the full UV-visible spectrum region of light to produce appreciable  $\text{H}_2$  from the water and methanol mixture.

## 2. Experimental procedure for the preparation of Au-loaded, graphene-supported $\text{TiO}_2$ nanocomposites as photocatalysts

### 2.1. Synthesis of graphene oxide sheets

Graphene oxide sheets (GOs) were synthesized from commercial graphite flakes by using a well-known modified Hummers method [28]. In a typical process, a mechanically combined mixture of graphite flakes (2 g) and  $\text{NaNO}_3$  (1 g) was put into concentrated  $\text{H}_2\text{SO}_4$  (46 mL, 18 M) at  $0^\circ\text{C}$  in an ice bath, and then  $\text{KMnO}_4$  (6 g) was slowly added to the resultant solution while stirring vigorously to keep the reaction temperature below  $20^\circ\text{C}$  in the ice bath so as to produce the graphite oxide. The reaction mixture was warmed to  $35^\circ\text{C}$  in an oil bath and maintained at this temperature with stirring until a brown-colored paste formed ( $\sim 2$  h).

Next, the reaction was terminated slowly by adding water (92 mL), which increased the temperature to between  $95$  and  $98^\circ\text{C}$ , and the resulting suspension was maintained at this temperature for 20 min. The suspension was then diluted to approximately 280 mL by the addition of water followed by treatment with  $\text{H}_2\text{O}_2$  (9 mL, 35%). Upon treatment with peroxide, the suspension turned bright yellow. After cooling in air, the suspension was filtered and washed with aqueous  $\text{HCl}$  (1:10, 37%) and then with water. The obtained solid was graphite oxide. The graphite oxide was further exfoliated by sonicating in water for 2 h and then centrifuged at 4500 rpm for 20 min. The supernatant was decanted and dried with a rotovapor at  $40^\circ\text{C}$  followed by vacuum drying at  $40^\circ\text{C}$  for 12 h. The obtained powder was GO.

### 2.2. Preparation of rGO- $\text{TiO}_2$ composites

Different amounts of  $\text{TiO}_2$  (P25) loaded with reduced graphene oxide (rGO) nanosheets were prepared via a hydrothermal synthesis process. In this process, the selective volumes of exfoliated aqueous GO suspension (stock solution,  $0.5 \text{ mg ml}^{-1}$ ) were re-exfoliated in a solution of distilled water (80 mL) and ethanol (40 mL) by ultrasonic treatment for 2 h. Then the 1 g  $\text{TiO}_2$  powder was slowly dispersed into the GO solution by stirring and stirred for another 2 h to get a homogeneous suspension. Sixty mL of the suspension was transferred to a 100 mL Teflon-sealed autoclave. The hydrothermal treatment was carried out at  $180^\circ\text{C}$  for 5 h to simultaneously reduce the GO into rGO in the presence of ethanol and anchor the  $\text{TiO}_2$  on the rGO active sites.

Finally, the resulting composite was recovered by rinsing several times with deionized water followed by ethanol and dried in an oven at  $40^\circ\text{C}$  for 12 h. The weight percentages of GO to  $\text{TiO}_2$  were 0, 0.25, 0.5, 1.0, 2.0, and 4.0%, and the composites were labeled as rGOXT (where X = 0, 0.25, 0.5, 1.0, 2.0, and 4.0).

### 2.3. Preparation of Au-loaded rGO- $\text{TiO}_2$ composites

A photodeposition process was used to prepare the Au-loaded rGOXT composites in the presence of UV irradiation. The

photodeposition was carried out in a well-shaped, double-walled quartz reactor. First, the rGOXT composites of 200 mg were dispersed in 300 ml water and methanol solution ( $v^{-1}=2:1$ ); then an appropriate amount of  $\text{AuCl}_3$  (4.36 mM) precursor solution was injected drop by drop with a syringe into the reactor. The reactor was sealed with a rubber septum and degassed by purging Ar in the solution for 30 min at atmospheric pressure. After degassing, the mixture was irradiated by using a high pressure 450 W Hg lamp for 1 h under vigorous stirring to obtain Au-loaded rGOXT composites. These samples were labeled as AuYrGOXT (where  $X=1.0$  and  $Y=0.5, 1.0, 2.0, 3.0, 4.0, 5.0$ , and  $8.0$  wt%).

### 3. Characterizations

#### 3.1. Structural characterization

Phase analysis was performed by using powder x-ray diffraction (XRD) with a Bruker D8-Advance x-ray diffractometer and monochromatized  $\text{Cu K}\alpha$  radiation ( $\lambda=1.5418 \text{ \AA}$ ). Transmission electron microscopy (TEM) images were collected on a Philips microscope with an accelerating voltage of 100 kV. Diffuse reflectance UV-visible spectra were obtained over the 200–800 nm range by setting  $\text{BaSO}_4$  as a reference and using a Carry 500 Diffuse reflectance UV-visible spectrophotometer (DRUVS). Diffuse reflectance Fourier transform infrared spectroscopy (FTIR) spectra were recorded via a Nexus 670 Nicolet spectrophotometer, Agilent Technology, USA, over a range of  $500\text{--}4000 \text{ cm}^{-1}$ . The room-temperature Raman spectra were obtained with an iHR550 Raman spectrophotometer, Horiba Jobin Yvon, with a HeNe laser (632.8 nm) as the excitation source. Brunauer-Emmet-Teller (BET) measurements of surface area and pore size distribution of nanocomposites were determined by using a Quantachrome NOVA 1200  $\text{N}_2$  gas adsorption/desorption analyzer at liquid nitrogen temperature.

#### 3.2. Photocatalytic hydrogen evolution from water splitting

The photocatalytic  $\text{H}_2$ -evolution reaction was carried out in a well-shaped, double-walled quartz reactor (outer diameter 50 mm) connected to a closed gas circulation, evacuation, and cooling system [29, 30]. A high-pressure 450 W Hg lamp was used as a UV-visible light irradiation source. In a typical experiment, 200 mg of rGOXT nanocomposite photocatalyst was suspended in a 340 mL of aqueous solution containing 10% methanol scavenger by volume. Prior to the photocatalytic reaction, the suspension of the catalyst was dispersed in an ultrasonic bath for 10 min and then purged with Ar through the reactor for 30 min to completely remove the dissolved oxygen and ensure that the reactor was in an anaerobic condition.

A continuous magnetic stirrer was applied at the bottom of the reactor to keep the photocatalyst particles in suspension during the whole experiment. The photocatalyst was irradiated by inserting a lamp into the center of the reactor. The temperature of the reactant solution was maintained at room

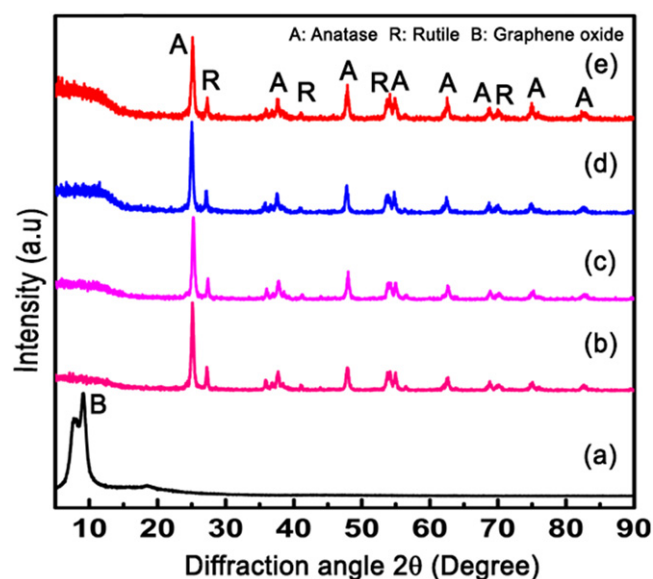


**Figure 1.** Powder x-ray diffraction patterns of (a) GO, (b) rGO0.25T, (c) rGO0.5T, (d) rGO1T, and (e) rGO2T samples.

temperature by providing a flow of cooling water through the outer wall of the reactor during the photocatalytic reaction. The reaction was carried out for 5 h, and the reaction products were analyzed by GC using an online sampling loop at intervals of 1 h. The GC (GOW-MAC 580 model) system was equipped with an All Tech molecular 80/100 sieve 5 A column and a thermal conductivity detector, with Ar flowing as the carrier gas. A similar process was used to prepare the Au-loaded rGOXT samples for  $\text{H}_2$  evolution.

### 4. Results and discussion

#### 4.1. Phase analysis

Powder XRD patterns of GO and rGOXT composites (where  $X=0, 0.25, 0.5, 1.0$ , and  $2.0$ ) are shown in figure 1. The XRD peak observed in figure 1(a) at about  $9.8^\circ$  corresponds to the (002) interlayer spacing ( $d$ ) of 0.90 nm, which fairly well matches the value reported in the literature for GO [22], whereas the XRD patterns of rGOXT composites shown in figures 1(b)–(e) represent well-defined crystalline peaks of both the anatase and rutile phases of  $\text{TiO}_2$ . These peaks are consistent with the JCPDS no. 21-1272 for anatase and no. 21-1276 for rutile (see figure S1, available in the supplementary data at [stacks.iop.org/NANO/25/265701/mmedia](http://stacks.iop.org/NANO/25/265701/mmedia)).

It is evident from the XRD that no characteristic diffraction peaks of reduced graphene (rGO) are observed in any composite samples (figures 1(b)–(e)). This might be because of the destruction of the regular stacking of GO through the reduction process under the hydrothermal conditions and the low amount of rGO or relatively low diffraction intensity of graphene [31, 32]. In addition, the change in the crystal structure of  $\text{TiO}_2$  after hybridization with GO nanosheets is observed to be almost negligible.

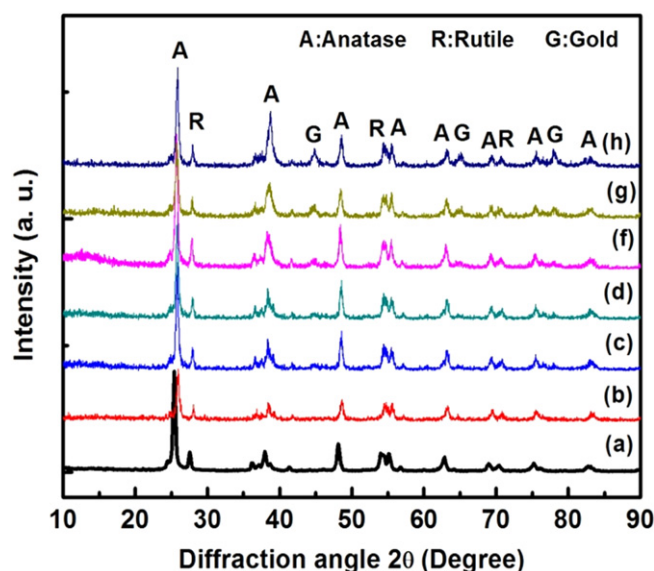


**Figure 2.** Powder x-ray diffraction patterns of (a) 0, (b) 0.5, (c) 1.0, (d) 2.0, (e) 3.0, (f) 4.0, (g) 5.0 and (h) 8.0 wt% of Au-loaded rGO1T samples.

The diffraction patterns of the rGO1T composites loaded with different Au contents (0.5–8.0 wt%) are shown in figure 2. In all samples (figures 2(b)–(h)), the peak positions shifted towards higher diffraction angles, which implies a reduction in  $d$ -value after incorporation of Au. The reduction of  $d$ -values represents Au loading on the  $\text{TiO}_2$ , which was expected in the present experiment. In sample Au0.5rGO1T (figure 2(b)), no Au peak is detected in XRD, which indicates the fine dispersion of Au species on the surface of rGO1T composites. However, the clear signatures of the Au peaks are observed in the sample containing Au contents from 1.0 to 8.0 wt% in rGO1T (figures 2(c)–(h)), which shows that Au nanoparticles have been photodeposited on rGO1T after UV light irradiation for 1 h.

#### 4.2. Raman spectra analysis of graphene and its composites

The crystalline quality and the degree of disorder of the carbon in the graphene structure after hydrothermal decompositions of pure and composite form were analyzed by using Raman spectroscopy. Significant structural changes occurred during the hydrothermal treatment of GO. The Raman spectra of GO,  $\text{TiO}_2$ , and rGOXT composites (where X = 0, 0.25, 0.5, 1.0, and 2.0) are demonstrated in figures 3(a)–(f). The two typical Raman bands in GO are observed at around 1351 and 1597  $\text{cm}^{-1}$  (shown in figure 3(a)). The band at around 1351  $\text{cm}^{-1}$  is common for disordered  $\text{sp}^2$  carbon and is known as the D-band [33, 34]. Another band at around 1597  $\text{cm}^{-1}$  is close to well-ordered graphite and is often called the G-band or  $\text{E}_{2g}$  mode [32, 33].

In the case of rGO0T (figure 3(b)), the anatase phase shows major Raman bands at 144, 395, 515, and 638  $\text{cm}^{-1}$ . These bands can be attributed to the five Raman-active modes of the anatase phase with the symmetries of  $\text{E}_{g(1)}$ ,  $\text{B}_{1g(1)}$ ,  $\text{A}_{1g} + \text{B}_{1g(2)}$ , and  $\text{E}_{g(2)}$ , respectively. The typical Raman bands

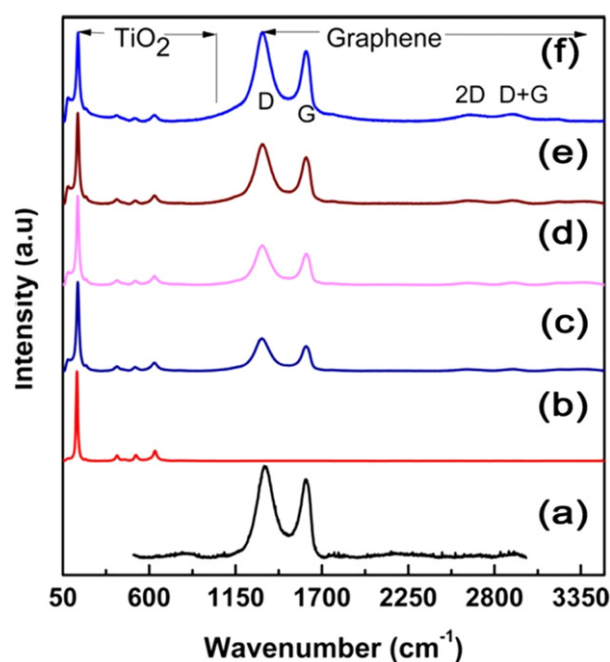


**Figure 3.** Raman spectra of (a) GO, (b) rGO0T, (c) rGO0.25T, (d) rGO0.5T, (e) rGO1.0T, and (f) rGO2.0T samples.

resulting from the rutile phase appear at 143 (superimposed with the 144  $\text{cm}^{-1}$  band resulting from the anatase phase), 235, 445, and 612  $\text{cm}^{-1}$  and can be ascribed to the  $\text{B}_{1g}$ , two-phonon scattering,  $\text{E}_g$ , and  $\text{A}_{1g}$  modes of the rutile phase, respectively [35–37].

All the Raman bands for the anatase and rutile phases are retained in rGOXT as shown in figures 3(c)–(f). In the present study, the Raman analysis reveals the shift in the G-band from 1597 to 1587  $\text{cm}^{-1}$  and in the D-band from 1351 to 1321  $\text{cm}^{-1}$  after  $\text{TiO}_2$  loading. These shifts are consistent with previous reports [38, 39]. Moreover, the 2D band at around 2692  $\text{cm}^{-1}$  is also observed (see figure S2), indicating the reduction of GO and the formation of a graphene structure. The peak position of the 2D band is similar to that of a monolayer graphene [40, 41]. Furthermore, the small variation in the ratio of intensity of the D-band to that of the G-band ( $I_D/I_G$ ) (see table S3) of rGOXT in comparison with that of GO indicates the decrease in the average size of the in-plane  $\text{sp}^2$  domains upon reduction of the exfoliated GO and confirms that the rGOXT composites exist as  $\text{TiO}_2$ -loaded graphene sheets [35, 42].

Figure 4 (see figures S4 and S5) shows the Raman spectra of the nanocomposites with different Au loadings. A small amount of Au loading (0.5 wt.%) significantly enhances the Raman intensity of the  $\text{TiO}_2$  bands. The absorption at 144  $\text{cm}^{-1}$  indicates an anatase crystalline phase structure [43]. In Au2rGO1T samples, intensity of the anatase peak is enhanced approximately twofold at the nanohybrid junction points because of the localized SPR from the gold nanostructures (see figure S5).

When the Au loading is increased from 0.5 to 2.0%, the absorption becomes broader and stronger and shifts positively in position by 5  $\text{cm}^{-1}$ . This suggests increased crystalline



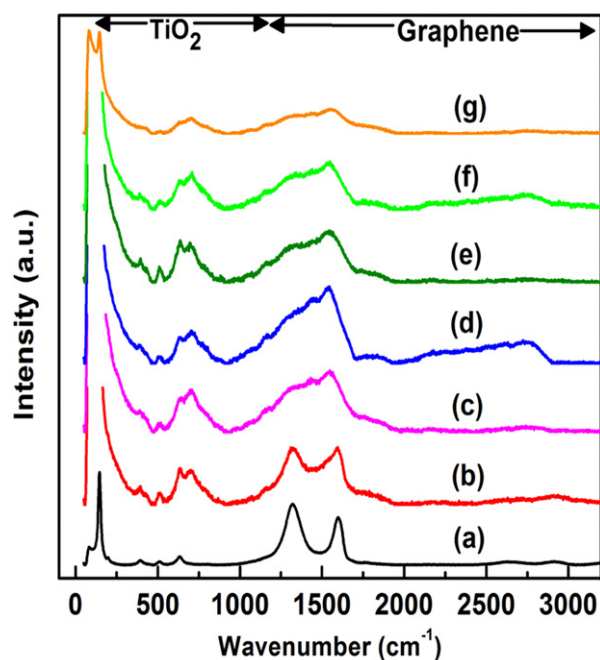


**Figure 4.** Raman spectra of (a) 0, (b) 0.5, (c) 1.0, (d) 2.0, (e) 3.0, (f) 5.0, and (g) 8.0 wt% of Au-loaded rGO1T samples.

defects within the phase [43]. Such defects may favor capturing photoelectrons and inhibiting charge recombination. Meanwhile, Au nanoparticles embedded within the structure may also serve as an electron conductor, which facilitates photoelectron transfer to the surface and further reduces the probability of charge recombination [44]. When Au content is further increased from 2.0 to 8.0%, the decrease in Raman peak intensity is observed. In addition, the Au-loaded rGO1T nanocomposites show reduction in the D-band and broadening in the G-band with respect to rGO1T, which is consistent with previous reported results [45]. The Au loading would cause broadening in the G-band as a result of electron–phonon coupling [45]. The intensity ratio of  $I_D/I_G$  is often used as a measure of defect levels in graphitic systems. The ratio of  $I_D/I_G$  is decreased from 1.28 to 0.48 up to 2.0 wt% Au (see table S3), indicating the increase in size of the  $sp^2$  domain during the UV treatment.

#### 4.3. Structural observation

Figure 5 (see figure S6) shows the TEM images of the rGO,  $TiO_2$  (rGO0T), rGO0.5T, rGO1T, rGO2T, and rGO5T samples. In figure 5(a), a crumpled, micrometer-long, two-dimensional morphology of an rGO sheet is observed after the hydrothermal treatment of GO in the presence of ethanol. The crumpling in the graphene sheet results from the retention of a thermodynamically stable, three-dimensional structure in a localized region from the thermodynamically unstable, two-dimensional sheet grown without substrate [33, 34]. Moreover, the size of the  $TiO_2$  nanoparticles normally ranges from 10 to 20 nm (figure 5(b)), which is consistent with the crystallite size of from 10 to 18 nm calculated from the XRD (see figure S1).

Figures 5(c) and (d) shows that the rGO provides good support for the densely distributed  $TiO_2$  nanoparticles on its surface. The dense distribution and loading of  $TiO_2$  nanoparticles on the rGO results from interfacial interaction and preferential heterogeneous nucleation between the hydrophilic functional groups (e.g.,  $-OH$ ,  $-COOH$ ) attached with GO and the hydroxyl groups on  $TiO_2$ .

Furthermore, the heterogeneous nucleation resulting from the different nucleation growth rate of hydrophilic functional and hydroxyl groups can also alleviate the crumpling and agglomeration of graphene nanosheets in a localized region. This intimate interaction facilitates an easy transfer of electrons from  $TiO_2$  nanoparticles to graphene sheets during the photo-excitation process. Moreover, figures 5(e) and (f) shows that the  $TiO_2$  nanoparticles are well covered by the rGO sheets.

The TEM image of photo-deposited Au (with contents 1.0–8.0 wt%) on the rGO1T samples is shown in figure 6 (and figure S7). The images reveal that Au is well loaded and dispersed on the  $TiO_2$ /graphene surface. As shown in figure 6(b), Au particles of mean size ranging from 3 to 8 nm of nearly spherical shape were observed as dark spots having obvious contrast with the  $TiO_2$ /graphene support. With increasing Au contents, the size of the Au particles increased, as expected. The Au loading of 8.0 wt% shows the cluster formation of Au nanoparticles on the  $TiO_2$  and rGO surface in figure 6(f). Here, the crumpled rGO sheet enables the formation of an interlocked network with Au and  $TiO_2$ . Akhavan has also found a similar kind of interlocked network formation in photodegraded graphene oxide sheets at the tip of ZnO nanorods [46]. This kind of nanocomposite nanolayer is desirable for the enhancement of the interfacial interaction between the co-catalysts and  $TiO_2$  and for the increase in the number of catalytically active sites on the co-catalyst surface.

#### 4.4. Specific surface area analysis

The nitrogen adsorption-desorption isotherms analysis was performed to investigate the porosity and BET surface area of the prepared samples. The TEM images (figures 5(b) and (d)) show an assembly of numerous particles with large open packing. The adsorption-desorption isotherms of the pure  $TiO_2$  (rGO0T) and GO supported  $TiO_2$  (rGO1T) are portrayed in figures 7(a) and (b), respectively. Nitrogen adsorption-desorption isotherm curves of these two samples show similarly shaped hysteresis loops at relative pressure ( $P/P_0$ ) close to unity. According to IUPAC, these curves fairly well display the typical type IV isotherms and type H3 hysteresis loops that are a characteristic feature of the mesopores [47–49]. Here, the mesopores formation is associated with the presence of aggregates of plate-like particles, giving rise to slit-like pores [47], as is consistent with the TEM results (figures 5(b) and (d)).

The pore size distribution curves of both samples (displayed in the inset of figure 7) are broad, ranging from 2 to over 100 nm (see figure S8) centered at 3.5 nm, which supports the existence of mesopores and macropores. In fact, the mesopores and macropores are formed as a result of the

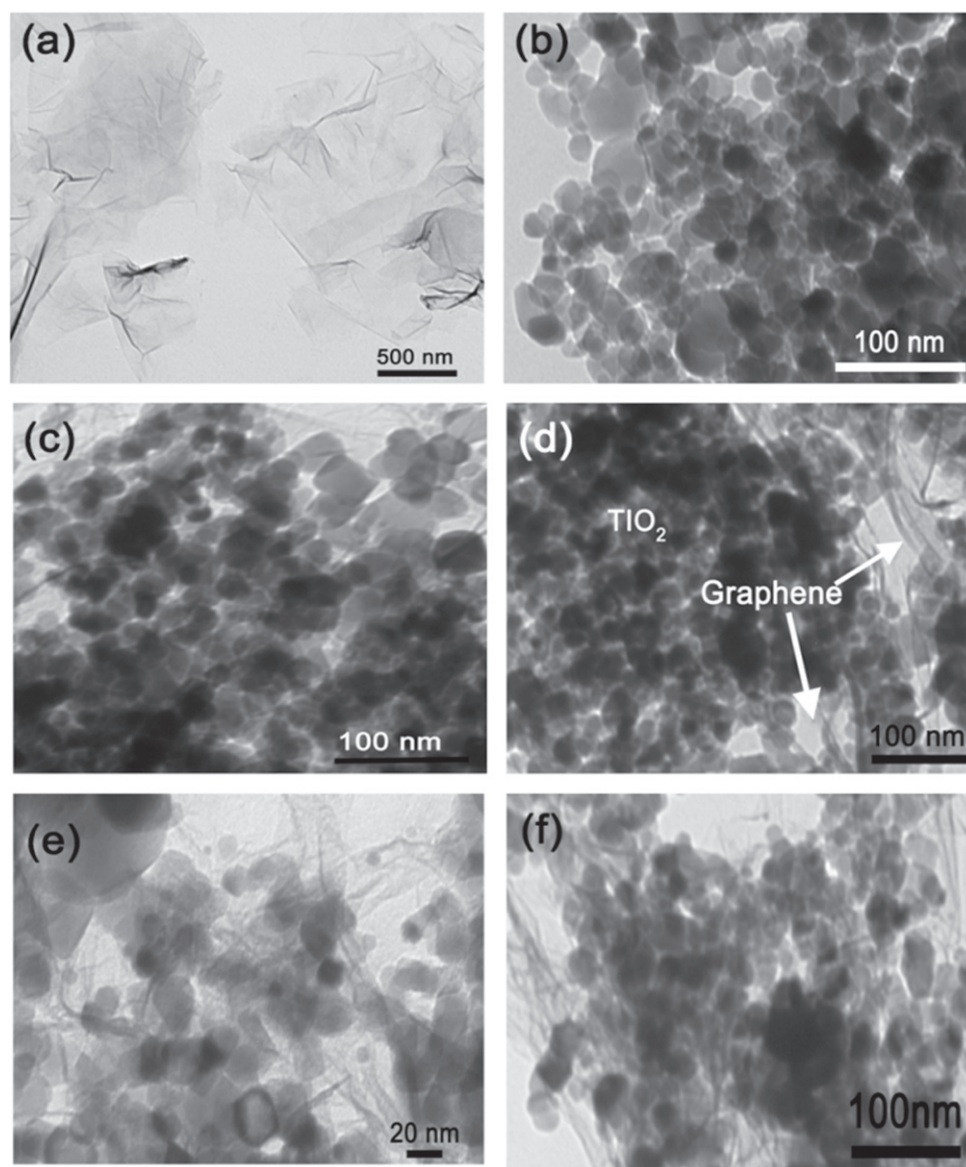


**Figure 5.** TEM images of (a) rGO, (b) rGO0T, (c) rGO0.5T, (d) rGO1T, (e) rGO2T, and (f) rGO5T samples.

aggregation of nanosheets, which occurs because the single-crystal nanosheets are nonporous [49]. Such organized porous structures might be extremely useful in photocatalysis because they possess efficient transport pathways to reactant and product molecules.

#### 4.5. UV-visible spectra of rGO-TiO<sub>2</sub> and Au-rGO-TiO<sub>2</sub> nanocomposites

The optical absorption properties of bare TiO<sub>2</sub> (rGO0T) and rGOXT samples measured with DRUVS are demonstrated in figure 8. The rGO0T sample shows the absorption in the UV region that is the characteristic feature of TiO<sub>2</sub> aroused as a result of the electron transitions from O<sub>2p</sub> → Ti<sub>3d</sub> level [25]. The presence of different amounts of rGO induces significant changes in the optical properties of photon absorption for TiO<sub>2</sub> in the rGOXT nanocomposites. The addition of rGO induces increased photon absorption intensity in the UV

region in all nanocomposites. This behavior is consistent with previous reports [50–52].

We believe that the increase in absorbance with the increase in rGO content in the rGOXT composite occurs as a result of the absorption contribution from rGO, the increase of the surface electric charge of the oxides, and the modification of the fundamental process of electron-hole pair formation during irradiation [53, 54]. Moreover, the rGO1T display the same absorption edge as rGO0.5T, implying that carbon was not much incorporated into the lattice of TiO<sub>2</sub> and that the graphene layer was only a substrate for immobilization of TiO<sub>2</sub> particles [55]. This is required to restrain the recombination of photo-excited electrons and holes during the photocatalytic water splitting for H<sub>2</sub> evolution. Further, the crossover of the rGO2T spectrum is observed. This is probably the result of the increase in opacity and scattering and to shielding of the TiO<sub>2</sub> surface from absorbing the photon in the presence of excess graphene. The shielding of the TiO<sub>2</sub>

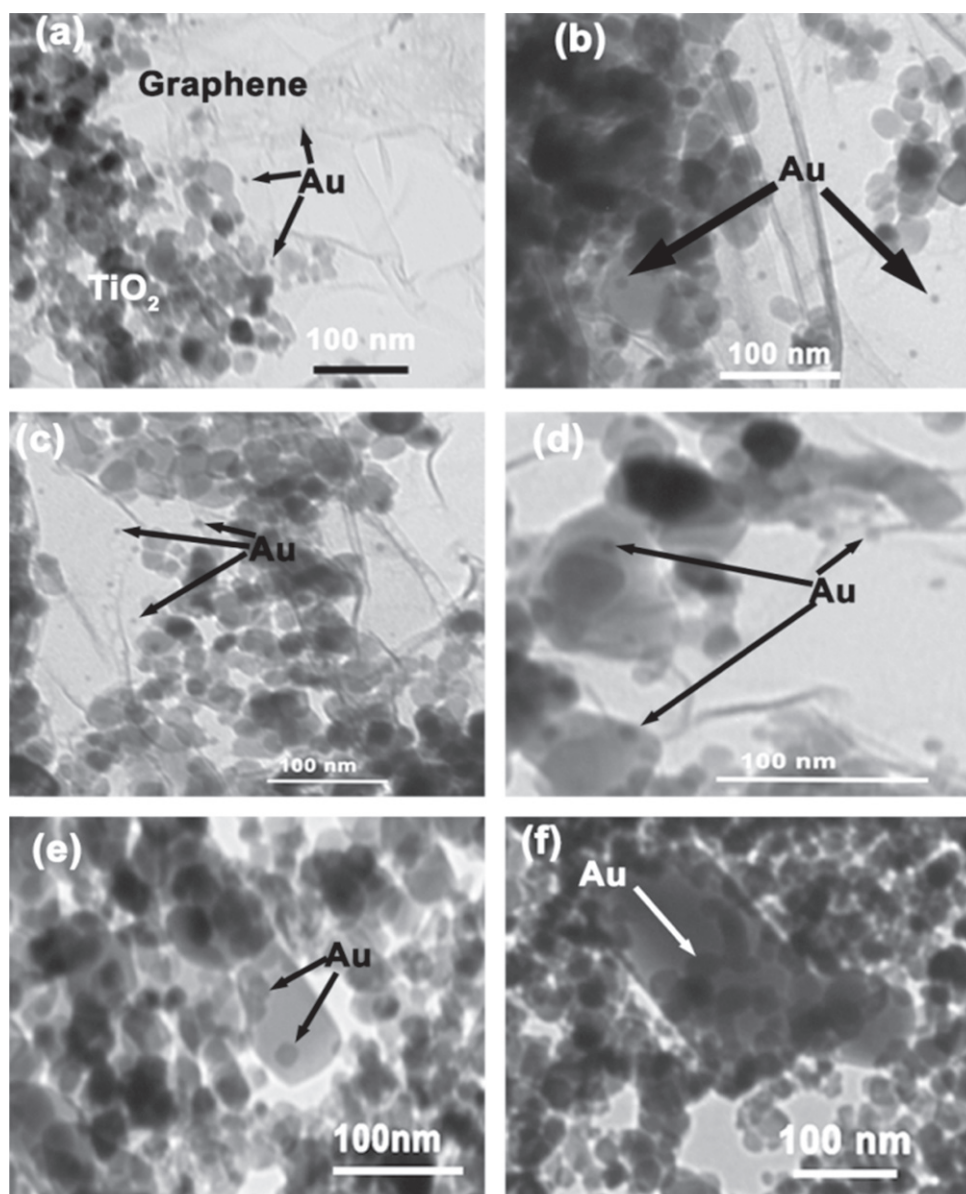


**Figure 6.** TEM images of Au contents of (a) 1.0, (b) 2.0, (c) 3.0, (d) 4.0, (e) 5.0, and (f) 8.0 wt% loaded on rGO/TiO<sub>2</sub> samples.

surface from the rGO is well observed in TEM images (figure 5(f)).

Furthermore, all rGOXT shows a broad absorption in the entire visible range because of the presence of graphenic carbons. The visible absorption background of rGOXT is increased with increases in the GO content because of the restoration of the  $\pi$ -electron conjugation within rGO sheets after hydrothermal reduction [56]. The absorption edge of rGOXT was red-shifted by 10–40 nm compared with that of pure TiO<sub>2</sub> (rGOOT), which indicates a narrowing of the band gap of TiO<sub>2</sub>.

This narrowing implies that GO with various oxygen-containing functional groups (see the FTIR spectra shown in figure S9) forms a surface complex with TiO<sub>2</sub> nanoparticles. Recently, it has been reported that the hydroxylated fullerene-(or fullerol-)TiO<sub>2</sub> complex and the carbon-doped TiO<sub>2</sub> composites absorb visible light because of the transfer of charge

onto the surface of the complex/composites [57, 58]. A similar charge-transfer complex can be formed between the rGO and TiO<sub>2</sub> surfaces. As a result of the surface complexation, the induced surface charge transfer in rGO/TiO<sub>2</sub> leads to the red shift seen by using DRUVS compared with bare TiO<sub>2</sub> because of the acidic functional groups present on GO (see figure S9).

Furthermore, the DRUVS spectra of Au-loaded rG1T samples are shown in figure 9. The plasmonic peak is observed around 552 nm, indicating the presence of Au nanoparticles in the Au-loaded rGO/TiO<sub>2</sub> samples. A significant enhancement in the absorption in the visible spectrum is observed. The enhancement in the absorption band is ascribed to the plasmonic resonance of metallic Au nanoparticles aroused from the collective oscillations of the free CB electrons induced by the incident electromagnetic radiation on Au nanoparticles [59]. The absorbance intensified and red-shifted



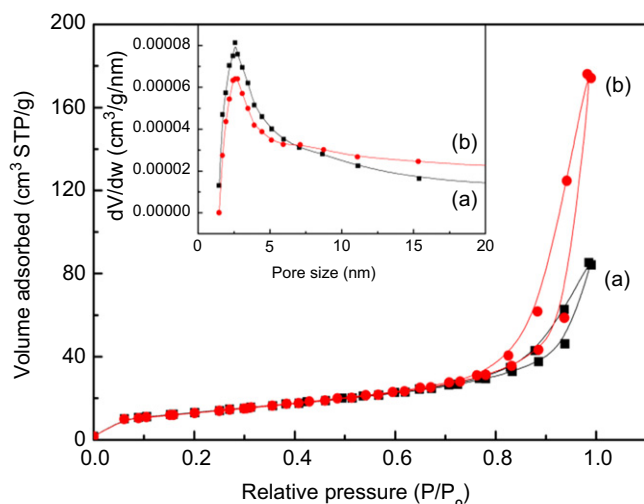


Figure 7. BET isotherm of (a) rGO0T and rGO1T samples.

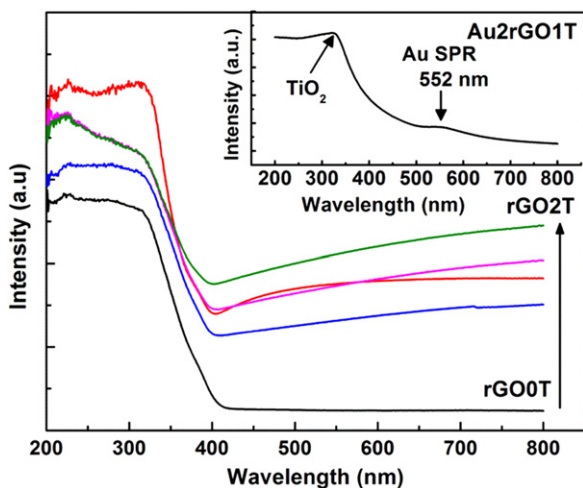


Figure 8. UV-Visible spectrum of rGOXT (where X=0, 0.25, 0.5, 1.0, and 2.0) samples.

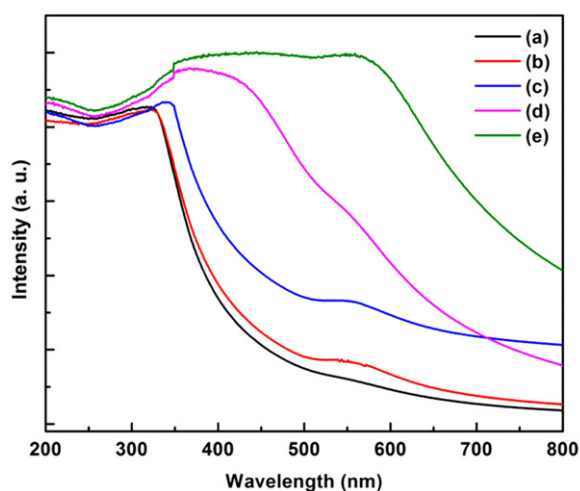


Figure 9. UV-Visible spectra of Au of (a) 0.5, (b) 1.0, (c) 2.0, (d) 5.0, and (e) 8.0 wt% loaded rGO1T samples.

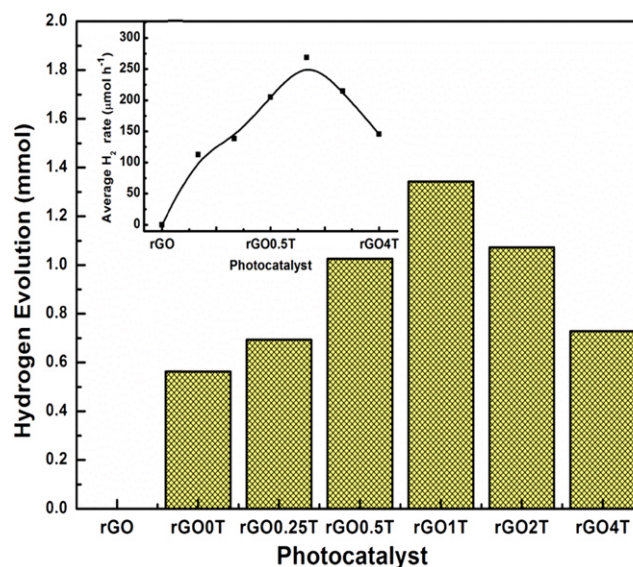


Figure 10. Photocatalytic activity of photocatalyst for H<sub>2</sub> evolution from methanol aqueous solution under UV-visible light irradiation.

with increasing Au loading as a result of the formation of bigger Au particles as observed in TEM images (see figure 6) [60] with different Au-loading contents.

#### 4.6. Photocatalytic hydrogen evolution from plasmonic active photocatalyst

Photocatalytic hydrogen (H<sub>2</sub>) evolution activities on reduced GO and its composite samples were evaluated through irradiation by high-pressure Hg Lamp in the UV-visible region in the presence of methanol as a scavenger. Figure 10 demonstrates the H<sub>2</sub> evolution value of the rGOXT composites. In a controlled reaction, H<sub>2</sub> evolution was almost negligible in the absence of a photocatalyst, whereas in the presence of a photocatalyst in solution, a significant H<sub>2</sub> evolution was detected. This indicates that the photocatalytic activity was happening as a result of the presence of the photocatalyst. In pure TiO<sub>2</sub> (rGO0T), the photocatalytic activity is observed to be very low, i.e., 0.56 mmol (i.e., 112 μmolh<sup>-1</sup>). The low activity results from the formation of fast recombination between CB electrons and valance band (VB) holes, and a fraction of the electrons and holes participate in the photocatalytic reaction [61, 62]. Also, the presence of a large over-potential in the production of H<sub>2</sub> on the TiO<sub>2</sub> surface and the fast backward reaction (recombination of hydrogen and oxygen into water) make TiO<sub>2</sub> inactive in photocatalytic water splitting in the absence of graphene.

However, the TiO<sub>2</sub> modified by small amount of graphene (rGO0.5T) shows considerable enhancement in the H<sub>2</sub> production rate, i.e., 1.8 fold (1.1 mmol) in comparison with pure TiO<sub>2</sub> (rGO0T). The further increase in the amount of graphene sheets accelerated the H<sub>2</sub> production and reached a maximum of 1.34 mmol (i.e., 268 μmolh<sup>-1</sup>), i.e., 2.4 fold over rGO1T, as shown in figure 10. Hence, the influence of graphene in photocatalytic activity reasonably reflects the enhancement in H<sub>2</sub> production. The enhancement in H<sub>2</sub>



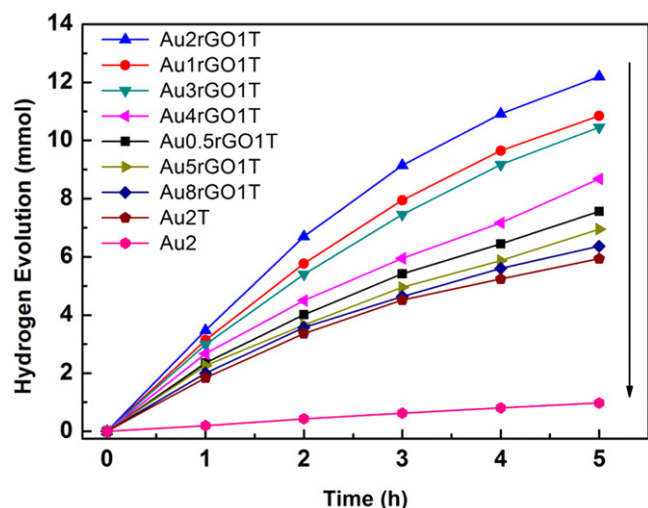


**Figure 11.** Hydrogen evolution through plasmonically active Au-loaded rGO1T photocatalysts from methanol aqueous solution under UV-visible light.

evolution in the presence of graphene in  $\text{TiO}_2$  could result from excellent electron-accepting and transferring capability and the capacity to restrain the recombination of the photo-excited electrons and holes effectively. It has been reported that the two-dimensional  $\pi$ -conjugation structure of graphene sheets facilitates the transfer of photo-induced electrons and can act as an excellent electron acceptor [63, 64].

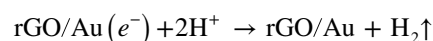
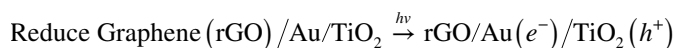
A further increase in graphene content leads to a reduction of the photocatalytic activity. Hence, in the present study, the critical or optimum value for good photocatalytic activity is 1.0 wt% of graphene with  $\text{TiO}_2$ . The graphene content  $\sim 2.0$  wt% shows a drastic decrease in photocatalytic activity in comparison with that of rGO1T. This probably results from the fact that the excess graphene screens the active sites on the surface of the  $\text{TiO}_2$  photocatalyst and shields them from incident photons. The screening of the surface of the  $\text{TiO}_2$  particles from rGO is observed in TEM images in figures 5(e) and (f). Hence, the screening prevents photon absorption onto the surface of the  $\text{TiO}_2$ , which results in a rapid reduction in the  $\text{H}_2$  production rate [65, 66]. No appreciable  $\text{H}_2$  evolution was detected with graphene as a photocatalyst under the same photocatalytic reaction conditions, which suggests that bare graphene is not active for photocatalytic  $\text{H}_2$  production under these experimental conditions. The results from this work and from past reports suggest that the loading of graphene onto the  $\text{TiO}_2$  surface is very important in deciding the optimal quantity of graphene for  $\text{H}_2$  production [61, 67].

To further enhance the capacity of  $\text{H}_2$  evolution by using photocatalysts, the plasmonic Au as a co-catalyst was loaded onto the optimal photocatalytically active rGO1T photocatalysts. The  $\text{H}_2$  generating capability of these photocatalysts was investigated in the same conditions. Figure 11 shows the photocatalytic activity of the rGO1T loaded with the Au co-catalyst (AuYrGO1T, where Y=0.5, 1.0, 2.0, 3.0, 4.0, 5.0, and 8.0 wt %) photocatalysts. In the Au0.5rGO1T sample, the  $\text{H}_2$  evolution value is 7 mmol (i.e.,  $1.4 \text{ mmol h}^{-1}$ ), which is 5.2 fold higher than for rGO1T, as shown in figure 10. The

maximum value of  $\text{H}_2$  production achieved was 12 mmol (i.e.,  $2.4 \text{ mmol h}^{-1}$ ) in Au2rGO1T. On the other hand, the Au contents above 2.0 wt% gradually decrease the  $\text{H}_2$  evolution activity.

Hence, it is observed that the  $\text{H}_2$  evolution activity was dramatically increased by increasing the Au contents up to the optimal value of 2.0%. This optimal value of the Au co-catalyst increases the trapping site for carriers like graphene as a result of the quantized charge effect. The trapping of carriers leads to a longer lifetime for the interfacial charge transfer [61–64]. The process involves the transfer of photo-generated electrons from the CB of  $\text{TiO}_2$  to co-catalysts such as graphene and Au, and the holes were scavenged by methanol in the VB of  $\text{TiO}_2$ . Hence, electrons and holes are efficiently separated. However, further increasing the Au loading on rGO1T results in a decrease of the  $\text{H}_2$  rate. This decrease is probably due to the increase in opacity and light scattering (see figure 11), which leads to a decrease of irradiation passing through the reaction suspension solution. Other possible explanations might be (i) the partial blockage of the  $\text{TiO}_2$  surface active sites as a result of excessive Au or reduction in average distance between trapping sites with increasing numbers of Au clusters confined within a particle and (ii) deterioration of the catalytic properties of Au metal nanoparticles as a result of their size enlargement [61, 68, 69].

The formation of the Au cluster or agglomeration of Au nanoparticles on a  $\text{TiO}_2$  surface is well observed in the TEM images in figures 6(d)–(f). Therefore, it is not surprising that the photocatalytic activity of rGO1T samples having an Au content of more than 2.0 wt% is lower. With higher Au content, there should be an inverse cosine dependence on the reciprocal of loading since the loaded metal particles merged together and the total periphery began to shrink [61]. The major reaction steps in this photocatalytic water-splitting mechanism under UV-visible light irradiation are summarized through the following mechanism.



#### 4.7. Charge transfer process in Au/graphene/ $\text{TiO}_2$ photocatalyst

Co-catalysts such as plasmonic Au and graphene improve the charge separation and suppress the recombination of excited photogenerated carriers and result in enhanced  $\text{H}_2$  evolution. Figure 12 demonstrates the charge separation and  $\text{H}_2$  evolution process. The whole process can be described as follows: It is well documented that semiconductor composites doped with noble metal or metal ions exhibit a negative shift in the Fermi level that implies a higher degree of electron accumulation in Au-loaded  $\text{TiO}_2$  [62, 70]. Thus, such a shift in the Fermi level improves the energetics of the composite system and enhances the efficiency of the interfacial charge-transfer process. These improvements are in turn associated with a considerable enhancement of the electric near-field.

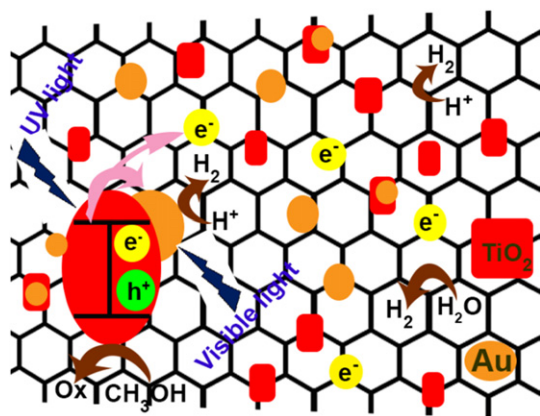


**Figure 12.** Charge transfer process in Au/graphene/TiO<sub>2</sub> photocatalyst.

This peculiar activity relates strongly to the size- and shape-dependent surface charge oscillation known as SPR in the presence of light irradiation [71, 72]. Here, the electrons in TiO<sub>2</sub> are excited from the VB to the CB by UV light irradiation. The excited electrons then migrate to the Au nanoparticle loaded on TiO<sub>2</sub>. Subsequently, the SPR effect (see figure 9) induced by appropriate visible light irradiation boosts the energy intensity of trapped electrons, resulting in the photocatalytic activity enhancement [73].

Furthermore, the incorporation of GO with TiO<sub>2</sub> creates the p-n junction, which also considerably improves the separation of photogenerated charges. The photogenerated holes are scavenged by methanol, and the electrons are excited to the CB. The electrons transferred from the CB of TiO<sub>2</sub> are injected into the reduced graphene in a graphene/TiO<sub>2</sub> system because the graphene/graphene-redox potential is slightly lower than the CB of TiO<sub>2</sub> [67, 74]. Graphene has a high charge carrier transfer and mobility as a result of its  $\pi$ -conjugate structure [75, 76], and hence the Au nanoparticles dispersed on the graphene sheet can also accept electrons and act as active sites to react with adsorbed H<sup>+</sup> ions for H<sub>2</sub> evolution (figure S10 presents the enhancement in H<sub>2</sub> evolution with Au contents).

In addition, some conduction electrons of TiO<sub>2</sub> likely transfer directly to the Au nanoclusters deposited on the surface of the TiO<sub>2</sub> semiconductor by ohmic interconnection or to carbon atoms on the graphene sheets, and the electrons then react with the adsorbed H<sup>+</sup> ions to form H<sub>2</sub>. Thus, the synergetic effect between the two co-catalysts, plasmonic Au nanoparticles and graphene, can effectively suppress photogenerated charge recombination, enlarge the active adsorption sites and reaction space, and consequently enhance the photocatalytic activity for H<sub>2</sub> evolution.

## 5. Conclusion

In summary, plasmonically active, Au-loaded graphene/TiO<sub>2</sub> composites photocatalysts were developed. The SPR on the metal-loaded photocatalysts can be an important way to use

the full spectrum in sunlight for solar energy harvest, especially for wide bandgap materials such as TiO<sub>2</sub>. Thus, both photon energies of UV and visible light can be absorbed and converted to chemical energy, i.e., H<sub>2</sub>, via water splitting. The optimal values of graphene and Au content were determined to be 1.0 and 2.0 wt%, respectively, and the corresponding hydrogen evolution rate to be enhanced by 268  $\mu\text{molh}^{-1}$  and 2.4  $\text{mmolh}^{-1}$ , respectively, compared with pure TiO<sub>2</sub>. The synergetic effect between the co-catalysts Au and graphene sheets can efficiently accept and transport the electrons from the excited semiconductor, suppress charge recombination, improve the interfacial charge transfer processes, and provide much more active adsorption sites and photocatalytic reaction centers, which consequently enhances the photocatalytic H<sub>2</sub> production activity. The Au nanoparticles are playing the role of electron acceptor as a result of the extra electromagnetic field provided by the SPR phenomenon.

## Acknowledgments

We thank Dr Bret N. Flanders, Dr Daniel L. Boyle, and Dr Leila Maurmann for helping us to obtain Raman spectra, TEM images, and FTIR, respectively. We also thank DST, New Delhi, Govt. of India, for providing us with the opportunity to visit KSU under a BOYSCAST fellowship.

## References

- [1] Paracchino A, Laporte V, Sivula K, Grätzel M and Thimsen E 2011 *Nat. Mater.* **10** 456
- [2] Hou Y D *et al* 2011 *Nat. Mater.* **10** 434
- [3] Kudo A and Miseki Y 2009 *Chem. Soc. Rev.* **38** 253
- [4] Maeda K *et al* 2010 *Angew. Chem., Int. Ed.* **49** 4096
- [5] Zhang J, Yu J G, Zhang Y M, Li Q and Gong J R 2011 *Nano Lett.* **11** 4774
- [6] Armaroli N and Balzani V 2007 *Angew. Chem. Int. Ed.* **46** 52
- [7] Dau H, Limberg C, Reier T, Risch M, Roggan S and Strasser P 2010 *Chem. Cat. Chem.* **2** 724
- [8] Grätzel M 2001 *Nature* **414** 338
- [9] Fujishima A and Honda K 1972 *Nature* **238** 37
- [10] Zhang X-Y, Li H-P, Cui X-L and Lin Y 2010 *J. Mater. Chem.* **20** 2801
- [11] Murdoch M, Waterhouse G I N, Nadeem M A, Metson J B, Keane M A, Howe R F, Llorca J and Idriss H 2011 *Nat. Chem.* **3** 489
- [12] Yu J G and Ran J R 2011 *Energy Environ. Sci.* **4** 1364
- [13] Carp O, Huisman C L and Reller A 2004 *Prog. Solid State Chem.* **32** 33
- [14] Khan Z, Khannam M, Vinothkumar N, Deb M and Qureshi M 2012 *J. Mater. Chem.* **22** 12090
- [15] Novoselov K S, Geim A K, Morozov S V, Jiang D, Zhang Y, Dubonos S V, Grigorieva I V and Firsov A A 2004 *Science* **306** 666
- [16] Geim A K and Novoselov K S 2007 *Nat. Mater.* **6** 183
- [17] Geim A K 2009 *Science* **324** 1530
- [18] Lv X-J, Zhou S-X, Zhang C, Chang H-X, Chena Y and Fu W-F 2012 *J. Mater. Chem.* **22** 18542
- [19] Wu Z S, Ren W, Wen L, Gao L, Zhao J, Chen Z, Zhou G, Li F and Cheng H M 2010 *ACS Nano* **4** 3187
- [20] Ng Y H, Iwase A, Kudo A and Amal R 2010 *J. Phys. Chem. Lett.* **1** 2607

- [21] Li Y, Wang H, Xie L, Liang Y, Hong G and Dai H 2011 *J. Am. Chem. Soc.* **133** 7296
- [22] Yeh T F, Syu J M, Cheng C, Chang T H and Teng H 2010 *Adv. Funct. Mater.* **20** 2255
- [23] Kowalska E, Remita H, Colbeau-Justin C, Hupka J and Belloni J 2008 *J. Phys. Chem. C* **112** 1124
- [24] Subramanian V, Wolf E and Kamat P V 2004 *J. Am. Chem. Soc.* **126** 4943
- [25] Zhang L, Yu J C, Yip H Y, Li Q, Kwong K W, Xu A W and Wong P K 2003 *Langmuir* **19** 10372
- [26] Gallo A, Marelli M, Psaro R, Gombac V, Montini T, Fornasiero P, Pievo R and Dal Santo V 2012 *Green Chem.* **14** 330
- [27] Yeh Y-C, Creran B and Rotello V M 2012 *Nanoscale* **4** 1871
- [28] Hummers W S and Offeman R E 1958 *J. Am. Chem. Soc.* **80** 1339
- [29] Kuo Y T, Frye C D, Ikenberry M and Klabunde K J 2013 *Catalysis Today* **199** 15
- [30] Kuo Y T and Klabunde K J 2012 *Nanotechnology* **23** 294001
- [31] Zhang H, Lv X J, Li Y M, Wang Y and Li J H 2010 *ACS Nano* **4** 380
- [32] Si Y C and Samulski E T 2008 *Chem. Mater.* **20** 6792
- [33] Nepal A, Singh G P, Flanders B N and Sorensen C M 2013 *Nanotechnology* **24** 245602
- [34] Xiang Q J, Yu J G and Jaroniec M 2011 *J. Phys. Chem. C* **115** 7355
- [35] Yu J G, Ma T T and Liu S W 2011 *Phys. Chem. Chem. Phys.* **13** 3491
- [36] Yu J G, Ma T T, Liu G and Cheng B 2011 *Dalton Trans.* **40** 6635
- [37] Yu J G, Fan J J and Cheng B 2011 *J. Power Sources* **196** 7891
- [38] Stankovich S, Dikin D A, Piner R D, Kohlhaas K A, Kleinhammes A, Jia Y, Wu Y, Nguyen S T and Ruoff R S 2007 *Carbon* **45** 1558
- [39] Lambert T N, Chavez C A, Hernandez-Sanchez B, Lu P, Bell N S, Ambrosini A, Friedman T, Boyle T J, Wheeler D R and Huber D J 2009 *J. Phys. Chem. C* **113** 19812
- [40] Vasu K S, Chakraborty B, Sampath S and Sood A K 2010 *Solid State Commun.* **150** 1295
- [41] Ferrari A C *et al* 2006 *Phys. Rev. Lett.* **97** 187401
- [42] Meyer J C, Geim A K, Katsnelson M I, Novoselov K S, Booth T J and Roth S 2007 *Nature* **446** 60
- [43] Parker J C and Siegel R W 1990 *Appl. Phys. Lett.* **57** 943
- [44] Li H, Bian Z, Zhu J, Huo Y, Li H and Lu Y 2007 *J. Am. Chem. Soc.* **129** 4538
- [45] Zhang H, Chen S, Quan X, Yu H T and Zhao H M 2011 *J. Mater. Chem.* **21** 12986
- [46] Akhavan O 2010 *ACS Nano* **4** 4174
- [47] Sing K S W, Everett D H, Haul R A W, Moscou L, Pierotti R A, Rouquerol J and Siemieniewska T 1985 *Pure Appl. Chem.* **57** 603
- [48] Kruk M and Jaroniec M 2001 *Chem. Mater.* **13** 3169
- [49] Rouquerol F, Rouquerol J and Sing K 1999 Adsorption by powders and porous solids: principles *Methodology and Applications* (San Diego: Academic Press)
- [50] Zhang H, Lv X, Li Y, Wang Y and Li J 2010 *ACS Nano* **4** 380
- [51] Wang Y J, Shi R, Lin J and Zhu Y F 2010 *Appl. Catal., B* **100** 179
- [52] Zhou K, Zhu Y, Yang X, Jiang X and Li C 2011 *New J. Chem.* **35** 353
- [53] Xu T G, Zhang L W, Cheng H Y and Zhu Y F 2010 *Chem. Rev.* **101** 38
- [54] Miyake Y and Tada H 2004 *J. Chem. Eng. Jpn.* **37** 630
- [55] Yu J G, Ma T T and Liu S W 2011 *Phys. Chem. Chem. Phys.* **13** 3491
- [56] Li D, Muller M B, Gilje S, Kaner R B and Wallace G G 2008 *Nat. Nanotechnol.* **3** 101
- [57] Park Y, Singh N J, Kim K S, Tachikawa T, Majima T and Choi W 2009 *Chem.—Eur. J.* **15** 10843
- [58] Sakthivel S and Kisch H 2003 *Angew. Chem. Int. Ed.* **42** 4908
- [59] Yonezawa T, Matsune H and Kunitake T 1999 *Chem. Mater.* **11** 33
- [60] Jensen T R and Duyne R P V 1999 *J. Phys. Chem. B* **103** 2394
- [61] Chen J-J, Wu J C S, Wu P C and Tsai D P 2011 *J. Phys. Chem. C* **115** 210
- [62] Choi H, Chen W T and Kamat P V 2012 *ACS Nano* **6** 4418
- [63] Zhang H, Lv X J, Li Y M, Wang Y and Li J H 2010 *ACS Nano* **4** 380
- [64] Yu J G, Wang W G, Cheng B and Su B L 2009 *J. Phys. Chem. C* **113** 6743
- [65] Yu J G, Hai Y and Jaroniec M 2011 *J. Colloid Interface Sci.* **357** 223
- [66] Yu J G, Hai Y and Cheng B 2011 *J. Phys. Chem. C* **115** 4953
- [67] Xiang Q, Yu J and Jaroniec M 2011 *Nanoscale* **3** 3670
- [68] Sreethawong T and Yoshikawa S 2005 *Catal. Commun.* **6** 661
- [69] Yu Z and Chuang S 2008 *Appl. Catal. B: Environ.* **83** 277
- [70] Jakob M, Levanon H and Kamat P V 2003 *Nano Lett.* **3** 353–8
- [71] Merlen A, Gadenne V, Romann J, Chevallier V, Patrone L and Valmalette J C 2009 *Nanotechnology* **20** 1
- [72] Wu D J, Xu X D and Liu X J 2008 *Solid State Commun.* **148** 163
- [73] Awazu K, Fujimaki M, Rockstuhl C, Tominaga J, Murakami H, Ohki Y, Yoshida N and Watanabe T 2008 *J. Am. Chem. Soc.* **130** 1676
- [74] Wang X, Zhi L J and Mullen K 2008 *Nano Lett.* **8** 323
- [75] Du X, Skacho I, Barker A and Anderi E Y 2008 *Nat. Nanotechnol.* **3** 491
- [76] Chen C, Cai W, Long M, Zhou B, Wu Y, Wu D and Feng Y 2010 *ACS Nano* **4** 6425